Open Science Discovery of Oral Non-Covalent SARS-CoV-2 Main Protease Inhibitor Therapeutics

The COVID Moonshot Consortium*

Abstract

The COVID-19 pandemic is a stark reminder that a barren global antiviral pipeline has grave humanitarian consequences. Future pandemics could be prevented by accessible, easily deployable broad-spectrum oral antivirals and open knowledge bases that derisk and accelerate novel antiviral discovery and development. Here, we report the results of the **COVID Moonshot**, a fully open-science structure-enabled drug discovery campaign targeting the SARS-CoV-2 main protease. We discovered a novel chemical scaffold that is differentiated to current clinical candidates in terms of toxicity and pharmacokinetics liabilities, and developed it into orally-bioavailable inhibitors with clinical potential. Our approach leverages crowdsourcing, high throughput structural biology, machine learning, and exascale molecular simulations. In the process, we generated a detailed map of the structural plasticity of the main protease, extensive structure-activity relationships for multiple chemotypes, and a wealth of biochemical activity data. In a first for a structure-based drug discovery campaign, all compound designs (>18,000 designs), crystallographic data (>500 ligand-bound X-ray structures), assay data (>10,000 measurements), and synthesized molecules (>2,400 compounds) for this campaign were shared rapidly and openly, creating a rich open and IP-free knowledgebase for future anti-coronavirus drug discovery.

Introduction

The development of broad spectrum oral antivirals is a critical but underexplored aspect of COVID-19 response and pandemic preparedness. Despite rapid progress in vaccine development, COVID-19 will likely become endemic[1], continuing to cause a significant number of deaths, especially in the Global South, unless there is an accessible treatment[2]. Antiviral therapeutics are a necessary and complementary strategy to vaccination in order to control COVID-19[3]. COVID-19 is not an isolated event, but the latest exemplar of a series of significant threats to human health caused by beta-coronaviruses also responsible for the SARS (2003) and MERS (2010) pandemics[4] . Open knowledge bases and technology infrastructures for antiviral drug discovery will enable pandemic preparedness by kindling the currently barren global antivirals' pipeline and providing multiple starting points for the development of therapeutics. Here, we report the open science discovery of a novel oral antiviral and a roadmap for the development of future SARS-CoV-2 and pan-coronavirus antivirals.

The SARS-CoV-2 main protease (Mpro; or 3CL-protease) is an attractive target for antiviral development due to its essential role in viral replication, a large degree of conservation across coronaviruses, and dissimilarity to human proteases[5] (**Supplementary FIgure 1**). Pioneering studies during and after the 2003 SARS pandemic established the linkage between Mpro inhibition and in vitro antiviral activity[6]. This is corroborated by recent in vitro and in vivo studies for SARS-CoV-2[7,8].

However, to warrant early use in the course of disease or even prophylactically among at-risk populations, an antiviral drug would need to be orally available with an excellent safety profile. Given the previous difficulties in developing peptidomimetic compounds into oral drugs, and the risk of downstream idiosyncratic hazards of covalent inhibition, we departed from the literature and chose to pursue novel non-covalent non-peptidomimetic scaffolds. Even though first-generation oral Mpro inhibitors are now in clinical trials[9,10] , there are still risks such that CYP3A4 inhibitor co-dosing may prove necessary for human exposure, and thus limit the use in at-risk populations due to potentially significant drug-drug Interactions. There remains a significant need for chemically differentiated oral antiviral protease inhibitors with the potential to rapidly enter clinical development.

*Authors are ordered alphabetically. For correspondence: john.chodera@choderalab.org (John Chodera); alpha.lee@postera.ai (Alpha Lee); nir.london@weizmann.ac.il (Nir London); frank.von-delft@diamond.ac.uk (Frank von Delft)

Crowdsourcing progression of X-ray fragment hits rapidly generated potent lead compounds with diverse chemotypes

The COVID Moonshot is an open science drug discovery campaign targeting SARS-CoV-2 Mpro[11,12], building off a rapid crystallographic and electrophilic fragment screening campaign that assessed 1495 fragment-soaked crystals screened within weeks to identify 78 hits that densely populated the active site (**Figure 1A**)[13]. This dataset was posted online on 18 Mar 2020, just days after the screen was completed[14]. The non-covalent fragment hits did not show detectable inhibition in a fluorescence based enzyme activity assay (indiciating IC_{50} > 100 μM). However, they provided a high-resolution map of key interactions that optimized compounds may exploit to inhibit Mpro.

Numerous approaches have been proposed to advance from fragments to lead compounds[15,16]. One strategy, *fragment merging*, aims to combine multiple fragments into a single more potent molecule, whereas *fragment expansion* elaborates a fragment to engage neighboring interactions. While these strategies are usually applied to a single fragment or a handful of fragments, our large-scale fragment screen produced a dense ensemble of hits, providing a unique opportunity for rapid lead generation by combining chemotypes from multiple fragments. Nonetheless, this requires heuristic chemical reasoning and spatial orientation of fragments in the binding site---a feat that can challenge algorithms but is potentially also solvable by humans. Building on successes in crowdsourced protein[17] and RNA[18] design campaigns, we hypothesized that crowdsourced human intuition and algorithmic strategies could accelerate the generation of potent lead compounds and furnish diverse chemical matter, as different chemists would employ different approaches and reasoning strategies.

We launched an online crowdsourcing platform [http://postera.ai/covid] on March 18th 2020 (**Figure 1B**), soliciting participants to submit compounds designed based on the fragment hits[12] . Data from biochemical assays are released regularly on the same platform, enabling contributing designers to build on all available data as well as contributed designs by others. Crucially, every design and all data are immediately disclosed, made openly available with no licensing or IP restrictions. This aggressive open science policy enables contributors to freely share their ideas. Within the first week, we received over 2,000 submissions, representing a diverse set of design strategies.

Gratifyingly, many submissions exploited spatially overlapping fragment hits. For example, the submission TRY-UNI-714a760b-6 was inspired by five fragments, furnishing a merged compound with IC_{50} of 21 uM (**Figure 1C**). This compound seeded the “aminopyridine” series, whose pursuit toward a preclinical candidate is described in detail below. Apart from the aminopyridine series, our campaign identified three additional chemically distinct lead series with measurable potencies inspired by reported SARS-CoV inhibitors (**Figure 1D**). Those compounds span the same binding pocket but feature different chemotypes, furnishing multiple backup series with different risk profiles. Subsequent to prepublication data disclosure from The COVID Moonshot, we were pleased to note that several efforts have been directed towards characterizing the Ugi[19] and the benzotriazole series we generated[20].

Figure 1: Crowdsourcing rapidly identified novel chemotype scaffolds by merging fragment hits.

A: The Diamond / XChem fragment screen that initiated this SARS-CoV-2 Mpro inhibitor discovery campaign generated 58 hits that completely cover the Mpro active site, with a variety of chemotypes engaging each pocket; 1495 X-ray datasets were collected and 78 solved structures for hits were publicly posted 18 Mar 2020[13].
The peptidomimetic N3 ligand is shown at left for comparison to indicate natural substrate engagement in the binding site, defining the peptide sidechain numbering scheme used throughout this work. The catalytic Cys145 cleaves the scissile peptide bond between P1 and P1', with His41-Cys145 forming a catalytic dyad whose coupled charge states that shuttle between zwitterionic and neutral states[21].
B: On March 18th 2020, the COVID Moonshot set up a crowdsourcing website to capture how to progress hits with measurable potency from fragments. We received over 2000 submissions in the first week.
C: Many submissions, such as TRY-UNI-714a760b-6, exploited spatially overlapping fragment hits to design potent leads that are also synthetically facile (see Figure 3).
D: Crowdsourcing efforts also identified three additional lead series inspired by reported SARS inhibitors, with measurable biochemical activity, and well-resolved engagement modes from high throughput crystallography.

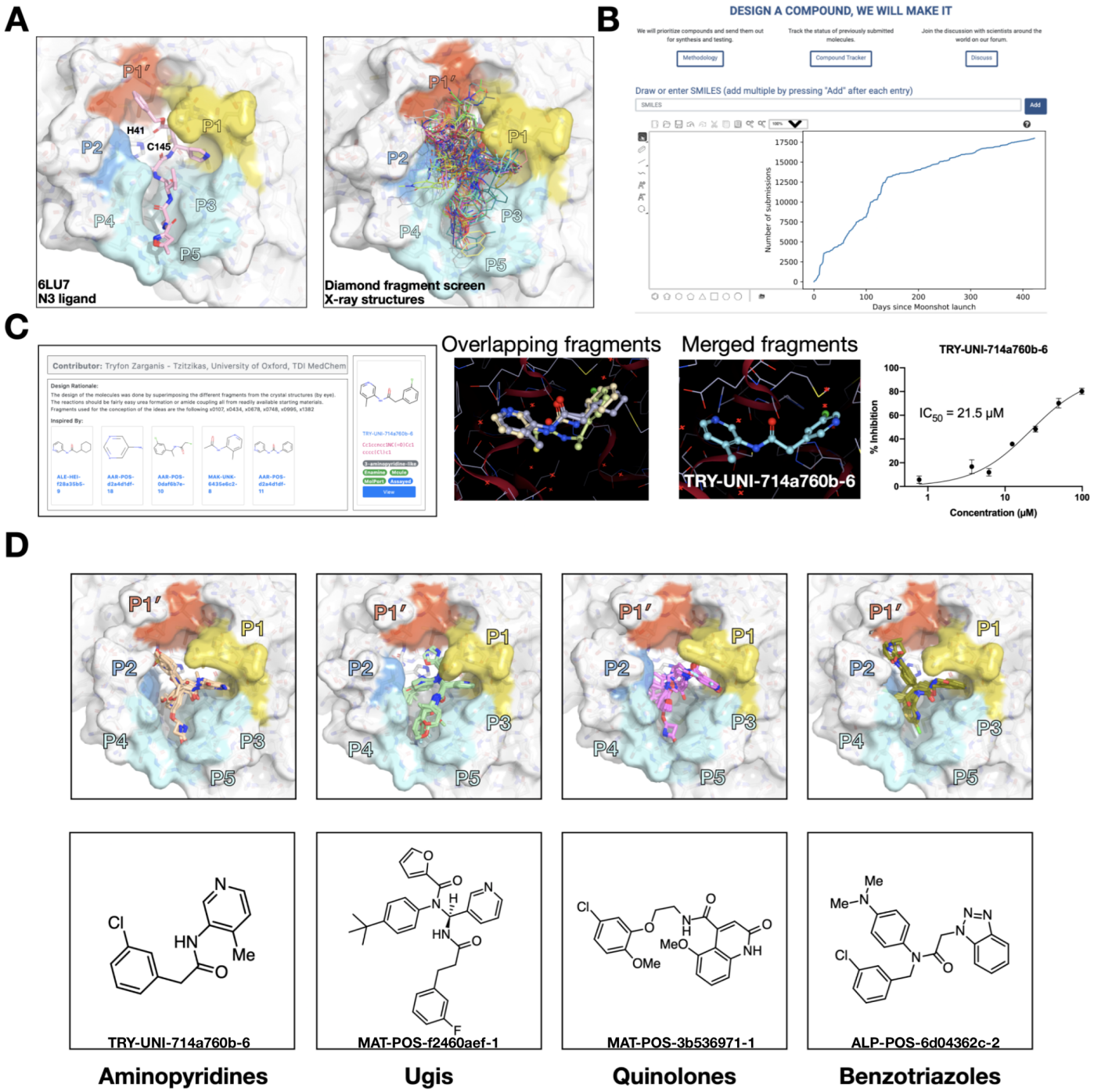

Machine learning and free energy perturbation enabled rapid optimization cycles

With a growing number of chemically diverse submissions aiming to progress multiple lead series, we next turned to computational methods to aid in triaging with the goal of increasing potency. To execute a rapid fragment-to-lead campaign, we use models to plan synthetic routes, enumerate synthetically accessible virtual libraries, and estimate potencies to prioritize which compounds to target for synthesis.

We used a machine learning approach to synthetic tractability[22,23] that plans efficient retrosynthetic routes capable of utilizing over 10 million advanced intermediates available from Enamine--a synthetic chemistry contract research organization (CRO) with one of the largest inventories of synthetic building blocks. The sheer number of building blocks, as well as the frequency in which building blocks go in and out of stock, presented the need for a rapid algorithmic approach to identifying compounds that could be quickly synthesized from available building blocks in a few reliable synthetic steps by chemists at Enamine. We automatically computed routes to all crowdsourced submissions. From the computed routes, synthetic complexity was estimated based on the number of steps and the probability of success of each step. The synthetic accessibility score, as well as the predicted synthetic route, were then used to aid medicinal chemistry decision making. **Figure 2A** (left) shows that our predicted synthetic complexity correlates with the actual time taken to synthesize target compounds. **Figure 2A** (right) demonstrates how the algorithm was able to pick out advanced intermediates as starting materials.

We estimated potency using alchemical free energy calculations[24–26] , an accurate physical modeling technique that has hitherto not been deployed in a high throughput setup due to its prohibitive computational cost. We employed Folding@Home[27] ---a worldwide distributed computing network where hundreds of thousands of volunteers around the world contributed computing power to create the world's first exascale computing resource[28]---to compute the free energy of binding of all 20,000+ crowdsourced submissions using the Open Force Field Initiative "Parsley" small molecule force fields[29] and nonequilibrium switching with the open source perses alchemical free energy toolkit[30] based on the GPU-accelerated OpenMM framework[31], culminating in over 1 ms of simulation time[28]. We first performed a small retrospective study using bioactivity data generated from the first week of crowdsourced compound designs, triaged solely using synthetic accessibility; **Figure 2B** shows that the results of these free energy calculations showed good correlation with experimentally-measured affinities. Henceforth, results from alchemical free energy calculations were published live, and used to guide compound selection and iterative design (see **Data Availability**).

Figure 2: **Machine learning route synthesis prediction enables rapid and inexpensive synthesis of compounds, while alchemical free energy calculations prioritizes potent compounds from large virtual synthetic libraries.**

A: Machine learning forecasts experimental synthesis time (left) and returns efficient routes that leverage over 10 million in-stock advanced intermediates (right). Our algorithm predicts the probability of each step being successful, and predicts synthetic accessibility by taking the product of the probabilities along the whole route. We analysed all compounds made in COVID Moonshot from 2020-09-01 to 2021-05-14. The right panel exemplifies the experimental execution of the predicted routes, demonstrating the ability of the algorithm to build on functionalized intermediates to shorten synthesis.
B: Applying alchemical free energy calculations at scale enables us to estimate the potency of compounds. The figure shows our automated free energy calculation workflow and retrospective evaluation on the first month of The COVID Moonshot data, which inspired confidence for large scale deployment during this campaign.

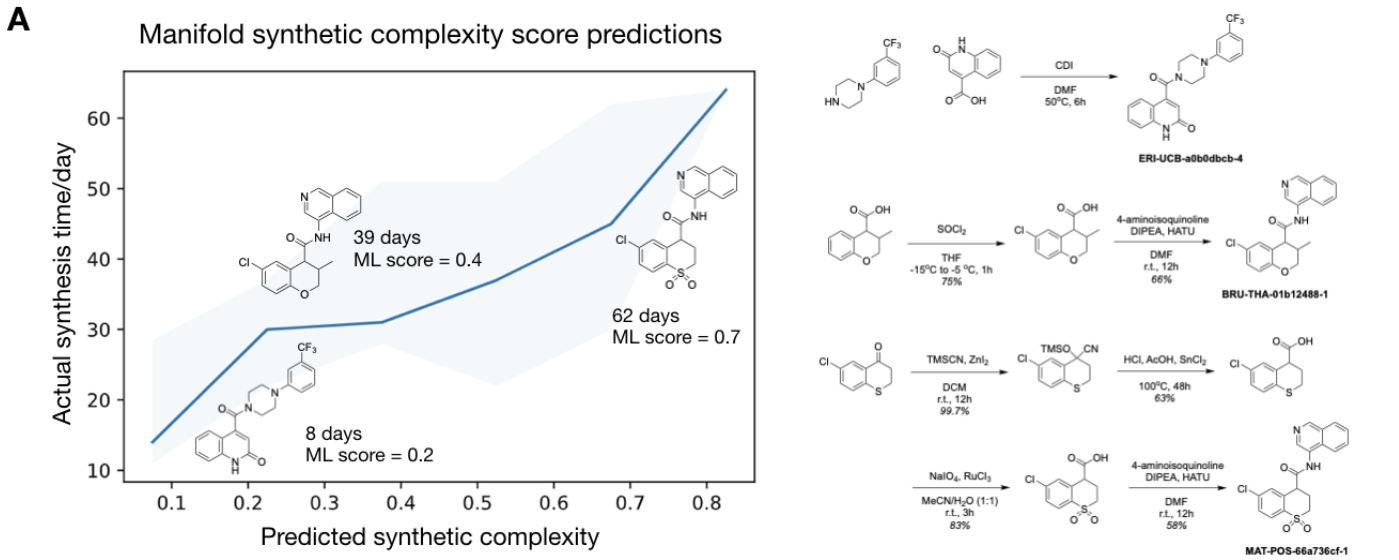

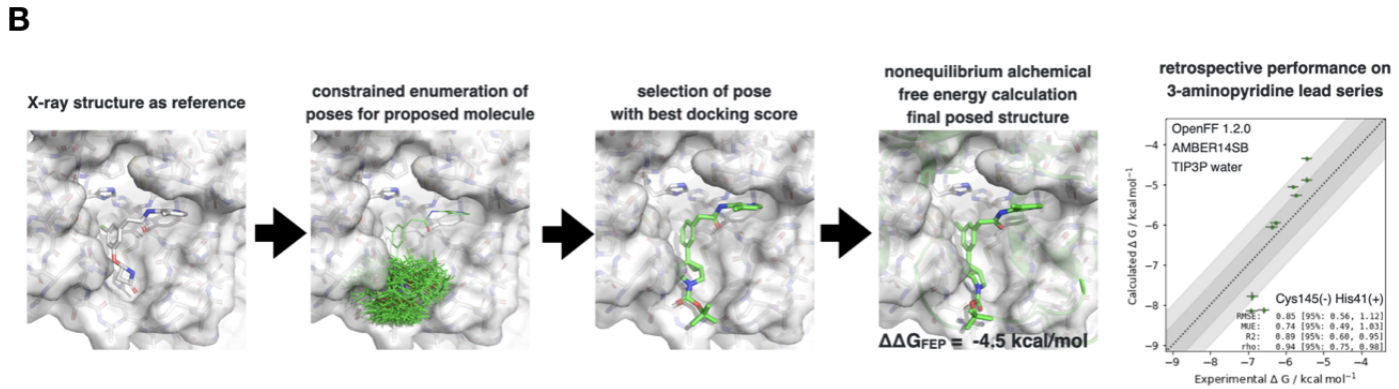

High-throughput structural biology uncovered binding modes and interactions underlying potency

Compounds selected based on synthetic accessibility and alchemical free energy calculations were synthesized and tested. We profiled every compound through crystal soaking and X-ray diffraction. Analysis of this large trove of structural data, totalling over 490 crystal structures, reveals the hotspots for ligand engagement and plasticity of each binding pocket. **Figure 3A** highlights the statistics of intermolecular interactions between the residues and our ligands across a preprocessed set of 391 complexes. The P1 and P2 pockets are the hotspots of interactions, yet the interaction patterns are starkly different. The salient interactions sampled by our ligands in the P1 pocket are H163 (H-bond donor), E166 (H-bond acceptor), S144 (H-bond donor), and N142 (hydrophobic interactions). Whereas P2 is dominated by π-stacking interactions with H41 and hydrophobic interactions M165. The P1' and P3/4/5 pockets are sparingly sampled by our ligands; the former can be targeted via hydrophobic interactions (T25), whereas the latter via H-bonds (Q192).

This pattern of intermolecular interactions is reflected in the plasticity of the different subpockets. The dominance of directional interactions in P1 renders it significantly more rigid than P2 (**Figure 3B**). Interestingly, this degree of rigidity is also dependent on the chemical series, with the Ugi and benzotriazole series being able to significantly deform the P2 pocket. Those series comprise more heavy atoms and span a larger region of the binding site, thus changes in P2 pocket interactions could be better tolerated.

Figure 3: High-throughput crystallography reveals hotspots for ligand engagement and structural plasticity of the binding sites.

A: The five subpockets exhibit different preferences for intermolecular interactions. The figure highlights the location of different types of interactions, with the shading indicating the frequency. The bottom column tallies the number of times each interaction was seen in our structures for different residues. The interaction map was generated using PLIPify and summarize the interactions witnessed across 391 complexes
B: The subpockets have different degrees of plasticity, which is also dependent on the chemical series. The corners of the figure shows the distribution of side chain RMSD deviations from the structure of PET-UNK-29afea89-2 (middle panel). The boxes exemplify ligands that significantly deform the pockets.

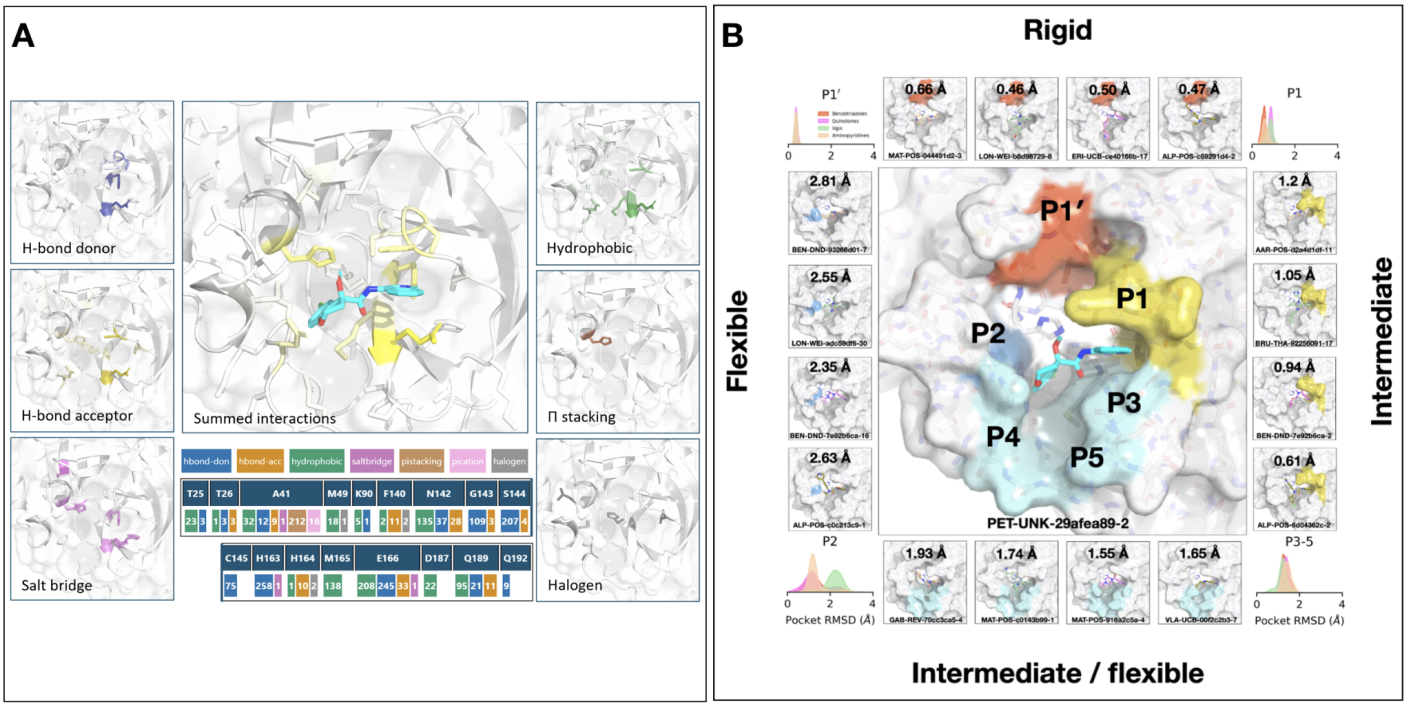

Design of an orally bioavailable inhibitor with potent antiviral activity

Our medicinal chemistry strategy was driven by the design of potent ligand-efficient and geometrically compact inhibitors that fit tightly in the substrate binding pocket. The former strategy aimed to increase the probability of achieving oral bioavailability, while the latter heuristic was motivated by the substrate envelope hypothesis for avoiding viral resistance[32]. **Figure 4A** shows that the P1 pocket admits a steep structure-activity relationship (SAR), perhaps unsurprising given its rigidity and preference for directional H-bond interactions (**Figure 3A**). A significant increase in potency was unlocked by replacing pyridine with isoquinoline, which picks up additional hydrophobic interactions with N142. The SAR around the P2 pocket is considerably wider, and broadly favours hydrophobic moieties. A step-change in potency was achieved by rigidifying the scaffold. We introduced the tetrahydropyran ring to transform the P2 substituent into a chromane moiety (compound MAT-POS-b3e365b9-1; the racemic mixture VLA-UCB-1dbca3b4-15, which was initially synthesized, has a pIC_{50} of 6.4), chosen because of building block availability. Despite possessing a degree of molecular complexity, MAT-POS-b3e365b9-1 is still a one-step amide coupling (**Figure 2A**). We finally explored the quaternary carbon centre, where the introduction of the methoxy group improves potency whilst decreasing the lipophilicity (ΔcLogP=-0.17). The 14 compounds shown on the selected “critical path” SAR (**Figure 4A**) came from 11 different designers and 8 different institutions, showcasing the wisdom of the crowd in action.

The ADME properties of PET-UNK-29afea89-2 revealed a metabolically unstable compound with high clearance in rodents, but less pronounced in human microsomes and hepatocytes (**Figure 4B**). We attempted to improve metabolic stability by investigating the simple strategy of lipophilicity reduction, exploring the P2 pocket as it exhibits the most tolerant potency SAR. We found that swapping from chloro to di-fluoro (MAT-POS-932d1078-3) leads to a slight decrease in potency but a significant increase in metabolic stability and oral bioavailability.

Our lead compound MAT-POS-932d1078-3 was subsequently profiled in SARS-CoV-2 antiviral assays across multiple cell lines, exhibiting EC50 of 126 nM in Calu-3 cells (**Figure 4C,** Supp Figure 2) and a reduction of intracellular viral RNA and infectious virus secretion into the apical compartment over 100-fold (**Figure 4D** and **E**). MAT-POS-932d1078-3 also exhibits properties required for an orally bioavailable therapeutic (see a broad set of physicochemical properties in Supp Table 1). Using the rat pharmacokinetics and in vitro human metabolism data, initial early projections suggest an oral human dose in the region 300 mg - 3g TID (three times a day). Studies are ongoing to both improve the precision of this prediction and fully explore the safety profile of current leads.

Figure 4: Iterative medicinal chemistry furnished an orally bioavailable lead compound.

A: Summary of the salient structure-activity relationship around the P1 and P2 binding pocket that improved potency in Mpro biochemical assay by 2.5 orders of magnitude.
B: Improving metabolic stability by tuning lipophilicity. The table shows in vitro and in vivo metabolism data for our lead compounds.
C: Our lead compounds exhibit strong antiviral activity against SARS-CoV-2. The figure shows the dose-response curve for a plaque reduction assay in the Calu-3 cell line. %UT is the % of infected cells normalized to untreated cells.
D: Intracellular viral RNA measured by qPCR at 96 hpi and **E**: plaque assay on Vero E6 cells of the apical medium at 96 hpi of kidney organoids infected with SARS-CoV-2 in the presence of 1 µM and 10 µM of MAT-POS-932d1078-3 and PET-UNK-29afea89-2 or DMSO. Data are mean and SD from a representative experiment of 2 independent experiments each performed with 2 biological replicates. Intracellular viral RNA levels in **D** were normalized to expression of the β-actin housekeeping gene.

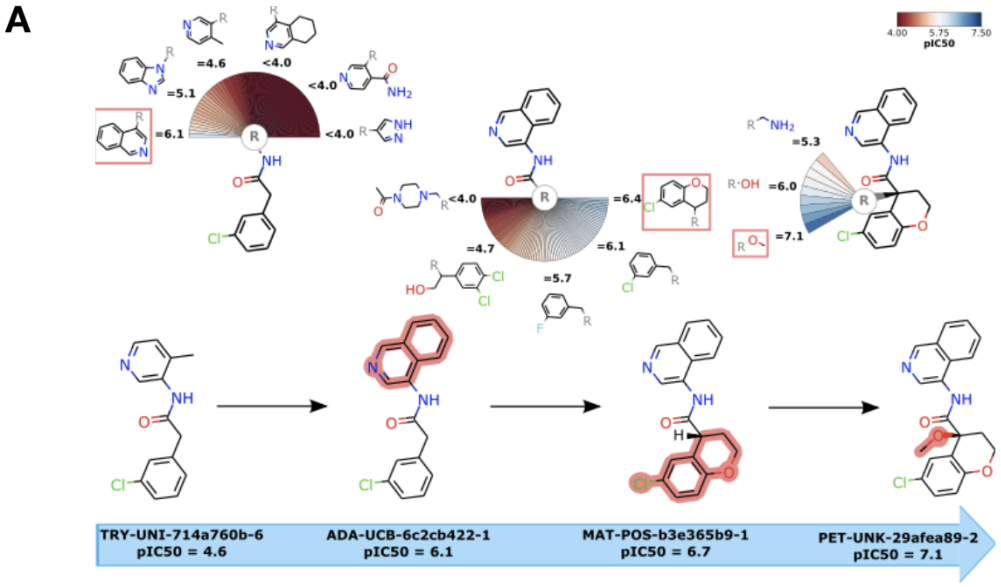

B

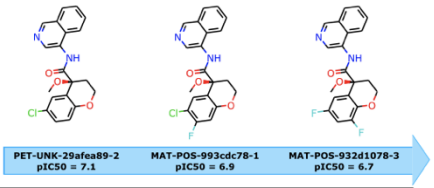

	PET-UNK-29afea89-2 pIC50 = 7.1	MAT-POS-993cdc78-1 pIC50 = 6.9	MAT-POS-932d1078-3 pIC50 = 6.7
Human Hepatocyte CLint: (µl/min/mg)	19.9	15.5	11.6
Human Microsome CLint: (µl/min/mg)	57.9	41.3	25.3
Rat Bioavailability (%)	14	40	25
Rat Fraction Unbound:	0.099	0.066	0.207
Rat IV CL: (ml/min/kg)	71.6	45.7	56.9
Rat CL(unbound): (ml/min/kg)	723.2	692.4	274.9

C

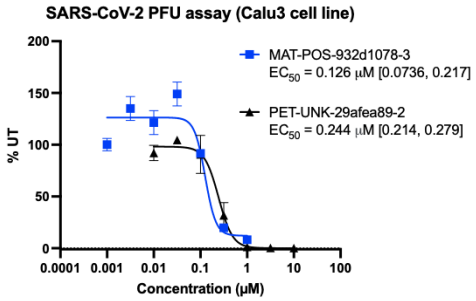

D

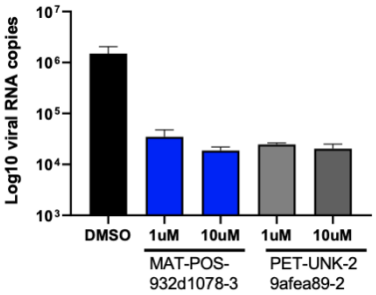

E

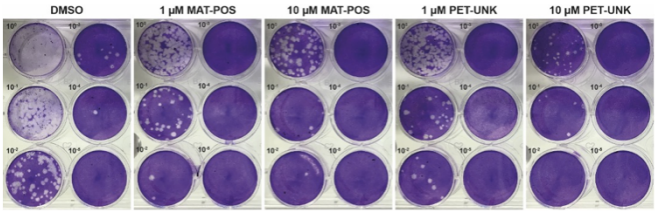

The COVID Moonshot presents a viable open science model for drug discovery

Herein, we report the success of an open science patent-free antiviral discovery program in rapidly developing an orally bioavailable antiviral in response to emergent pandemic threat in producing compounds poised to enter preclinical studies. As a result of the open science policy, a large number of collaborators were eager and able to provide in-kind support, providing synthesis, assays and in vitro/vivo experiments. By making all data immediately available, and all compounds purchasable from Enamine, we aim to accelerate research globally along parallel tracks following up on our initial work.

The COVID Moonshot and its lead compounds have been adopted into the drug development portfolio of the Drugs for Neglected Diseases Initiative (DNDi), having completed a successful philanthropic fundraise that enables IND-enabling studies and preparation for clinical trials. We envisage a direct-to-generics economic model, where the eventual drug price will reflect the cost of producing the compounds rather than the monopoly rent associated with holding intellectual property on the compound.

Open science efforts have transformed many areas of biosciences, with illustrious examples such as the Human Genome Project[33], the Structural Genomics Consortium[34] , and the RAS Initiative[35]. Yet its inroad in therapeutic discovery is slow because of the perceived need for commercial return. We hope The COVID Moonshot is an exemplar for open science drug discovery[36] that paves the way towards a new paradigm for infectious diseases drug discovery - a disease area of grave public importance but chronically underfunded by the private sector.

Materials and Methods

The Supplementary Material contains methods and protocols for all the experiments reported in this manuscript.

Data availability

- **All compound submissions and data (including HTS screen) are available via GitHub:** https://github.com/postera-ai/COVID_moonshot_submissions
- **All compound designs, datasets, and X-ray structures are indexed on the COVID Moonshot website:** https://postera.ai/covid
- **Bioactivity data can be interactively browsed at the COVID Moonshot website:** https://covid.postera.ai/covid/activity_data
- **Alchemical free energy calculations code and datasets are indexed on GitHub:** https://github.com/foldingathome/covid-moonshot
- **All X-ray structures are available for interactive viewing or bulk download on Fragalysis:** https://fragalysis.diamond.ac.uk/viewer/react/preview/target/Mpro

Resource availability

- Compounds: We have made all compounds assayed here current Enamine catalogue compounds, and readily available for purchase from Enamine (and other suppliers) via the Manifold platform accessible for each compound page on the COVID Moonshot website: https://covid.postera.ai/covid/activity_data

Acknowledgements:

The COVID Moonshot acknowledges funding by the Wellcome Trust on behalf of the Covid-19 Therapeutics Accelerator. The COVID Moonshot project is particularly grateful to UCB Pharma Ltd and

UCB S.A for the support from their Medicinal and Computational Chemistry groups, to Novartis International AG for generous in-kind ADME and PK contributions, Takeda for in-kind contribution of antiviral assays/pan-corona biochemical assays, and Nanosyn for protease panel assays. We thank CDD Vault and OpenEye Scientific for their in-kind contribution allowing the consortium to use their software. We also thank the citizen scientists of Folding@home for donating their computing resources.

Funding acknowledgments and Conflicts of Interest

Funding acknowledgement and CoI statements for each author is listed in the consortium spreadsheet (The COVID Moonshot Consortium).

References

1. Phillips, N. The coronavirus is here to stay - here's what that means. *Nature* **590**, 382–384 (2021).
2. Winchester, N. Covid-19 vaccinations: is the Global South falling behind? *UK House of Lords library* https://lordslibrary.parliament.uk/covid-19-vaccinations-is-the-global-south-falling-behind/ (2021).
3. Zhao, T. *et al.* Warnings regarding the potential coronavirus disease 2019 (COVID-19) transmission risk: Vaccination is not enough. *Infect. Control Hosp. Epidemiol.* 1 (2021).
4. de Wit, E., van Doremalen, N., Falzarano, D. & Munster, V. J. SARS and MERS: recent insights into emerging coronaviruses. *Nat. Rev. Microbiol.* **14**, 523–534 (2016).
5. Ullrich, S. & Nitsche, C. The SARS-CoV-2 main protease as drug target. *Bioorg. Med. Chem. Lett.* **30**, 127377 (2020).
6. Pillaiyar, T., Manickam, M., Namasivayam, V., Hayashi, Y. & Jung, S.-H. An Overview of Severe Acute Respiratory Syndrome-Coronavirus (SARS-CoV) 3CL Protease Inhibitors: Peptidomimetics and Small Molecule Chemotherapy. *J. Med. Chem.* **59**, 6595–6628 (2016).
7. Zhang, L. *et al.* Crystal structure of SARS-CoV-2 main protease provides a basis for design of improved α-ketoamide inhibitors. *Science* **368**, 409–412 (2020).
8. Jin, Z. *et al.* Structure of Mpro from SARS-CoV-2 and discovery of its inhibitors. *Nature* **582**, 289–293 (2020).
9. Study of pf-07321332 in healthy participants. https://clinicaltrials.gov/ct2/show/NCT04756531.
10. Study of PBI-0451 in Healthy Subjects. https://clinicaltrials.gov/ct2/show/NCT05011812.
11. von Delft, F. *et al.* A white-knuckle ride of open COVID drug discovery. *Nature* **594**, 330–332 (2021).
12. Chodera, J., Lee, A. A., London, N. & von Delft, F. Crowdsourcing drug discovery for pandemics. *Nat. Chem.* **12**, 581 (2020).
13. Douangamath, A. *et al.* Crystallographic and electrophilic fragment screening of the SARS-CoV-2 main protease. *Nat. Commun.* **11**, 5047 (2020).

14. Main protease structure and XChem fragment screen. *Diamond Light Source* https://www.diamond.ac.uk/covid-19/for-scientists/Main-protease-structure-and-XChem.html (2020).
15. Rees, D. C., Congreve, M., Murray, C. W. & Carr, R. Fragment-based lead discovery. *Nat. Rev. Drug Discov.* **3**, 660–672 (2004).
16. Erlanson, D. A., Fesik, S. W., Hubbard, R. E., Jahnke, W. & Jhoti, H. Twenty years on: the impact of fragments on drug discovery. *Nat. Rev. Drug Discov.* **15**, 605–619 (2016).
17. Cooper, S. *et al.* Predicting protein structures with a multiplayer online game. *Nature* **466**, 756–760 (2010).
18. Lee, J. *et al.* RNA design rules from a massive open laboratory. *Proc. Natl. Acad. Sci. U. S. A.* **111**, 2122–2127 (2014).
19. Kitamura, N. *et al.* Expedited Approach toward the Rational Design of Noncovalent SARS-CoV-2 Main Protease Inhibitors. *J. Med. Chem.* (2021) doi:10.1021/acs.jmedchem.1c00509.
20. Han, S. H. *et al.* Structure-Based Optimization of ML300-Derived, Noncovalent Inhibitors Targeting the Severe Acute Respiratory Syndrome Coronavirus 3CL Protease (SARS-CoV-2 3CLpro). *J. Med. Chem.* (2021) doi:10.1021/acs.jmedchem.1c00598.
21. Kneller, D. W. *et al.* Structural plasticity of SARS-CoV-2 3CL Mpro active site cavity revealed by room temperature X-ray crystallography. *Nat. Commun.* **11**, 3202 (2020).
22. Schwaller, P. *et al.* Molecular Transformer: A Model for Uncertainty-Calibrated Chemical Reaction Prediction. *ACS Cent Sci* **5**, 1572–1583 (2019).
23. Morris, A. *et al.* Discovery of SARS-CoV-2 main protease inhibitors using a synthesis-directed de novo design model. *Chem. Commun.* **57**, 5909–5912 (2021).
24. Mey, A. S. J. *et al.* Best Practices for Alchemical Free Energy Calculations. *arXiv [q-bio.BM]* (2020).
25. Abel, R., Wang, L., Mobley, D. L. & Friesner, R. A. A Critical Review of Validation, Blind Testing, and Real- World Use of Alchemical Protein-Ligand Binding Free Energy Calculations. *Curr. Top. Med. Chem.* **17**, 2577–2585 (2017).
26. Armacost, K. A., Riniker, S. & Cournia, Z. Exploring Novel Directions in Free Energy Calculations. *J. Chem. Inf. Model.* **60**, 5283–5286 (2020).
27. Shirts, M. & Pande, V. S. COMPUTING: Screen Savers of the World Unite! *Science* **290**, 1903–1904 (2000).

28. Zimmerman, M. I. *et al.* SARS-CoV-2 simulations go exascale to predict dramatic spike opening and cryptic pockets across the proteome. *Nat. Chem.* **13**, 651–659 (2021).
29. Qiu, Y. *et al.* Development and Benchmarking of Open Force Field v1.0.0, the Parsley Small Molecule Force Field. *ChemRxiv* (2020) doi:10.26434/chemrxiv.13082561.v2.
30. Rufa, D. A. *et al.* Towards chemical accuracy for alchemical free energy calculations with hybrid physics-based machine learning / molecular mechanics potentials. *bioRxiv* 2020.07.29.227959 (2020) doi:10.1101/2020.07.29.227959.
31. Eastman, P. *et al.* OpenMM 7: Rapid development of high performance algorithms for molecular dynamics. *PLoS Comput. Biol.* **13**, e1005659 (2017).
32. Nalam, M. N. L. *et al.* Evaluating the substrate-envelope hypothesis: structural analysis of novel HIV-1 protease inhibitors designed to be robust against drug resistance. *J. Virol.* **84**, 5368–5378 (2010).
33. Lander, E. S. *et al.* Initial sequencing and analysis of the human genome. *Nature* **409**, 860–921 (2001).
34. Williamson, A. R. Creating a structural genomics consortium. *Nat. Struct. Biol.* **7 Suppl**, 953 (2000).
35. U.S. Cancer Institute 'Megaproject' to Target Common Cancer-Driving Protein. *Science* https://www.science.org/content/article/us-cancer-institute-megaproject-target-common-cancer-driving-protein.
36. Lee, A., Chodera, J. & von Delft, F. Why we are developing a patent-free Covid antiviral therapy. *Knowable mag.* (2021) doi:10.1146/knowable-092721-1.
37. Malla, T. R. *et al.* Mass spectrometry reveals potential of β-lactams as SARS-CoV-2 Mpro inhibitors. *Chem. Commun.* **57**, 1430–1433 (2021).
38. Noske, G. D. *et al.* A Crystallographic Snapshot of SARS-CoV-2 Main Protease Maturation Process. *J. Mol. Biol.* **433**, 167118 (2021).
39. Winter, G. *et al.* DIALS: implementation and evaluation of a new integration package. *Acta Crystallogr D Struct Biol* **74**, 85–97 (2018).
40. Winter, G. *et al.* How best to use photons. *Acta Crystallogr D Struct Biol* **75**, 242–261 (2019).
41. Winter, G. & McAuley, K. E. Automated data collection for macromolecular crystallography. *Methods* **55**, 81–93 (2011).
42. Kabsch, W. Integration, scaling, space-group assignment and post-refinement. *Acta Crystallogr. D Biol. Crystallogr.* **66**, 133–144 (2010).

43. Winter, G., Lobley, C. M. C. & Prince, S. M. Decision making in xia2. *Acta Crystallogr. D Biol. Crystallogr.* **69**, 1260–1273 (2013).

44. Vonrhein, C. *et al.* Data processing and analysis with the autoPROC toolbox. *Acta Crystallogr. D Biol. Crystallogr.* **67**, 293–302 (2011).

45. Krojer, T. *et al.* The XChemExplorer graphical workflow tool for routine or large-scale protein-ligand structure determination. *Acta Crystallogr D Struct Biol* **73**, 267–278 (2017).

46. Pearce, N. M. *et al.* A multi-crystal method for extracting obscured crystallographic states from conventionally uninterpretable electron density. *Nat. Commun.* **8**, 15123 (2017).

47. Emsley, P., Lohkamp, B., Scott, W. G. & Cowtan, K. Features and development of Coot. *Acta Crystallogr. D Biol. Crystallogr.* **66**, 486–501 (2010).

48. Long, F. *et al.* AceDRG: a stereochemical description generator for ligands. *Acta Crystallogr D Struct Biol* **73**, 112–122 (2017).

49. Bruno, I. J. *et al.* Retrieval of crystallographically-derived molecular geometry information. *J. Chem. Inf. Comput. Sci.* **44**, 2133–2144 (2004).

50. Cottrell, S. J., Olsson, T. S. G., Taylor, R., Cole, J. C. & Liebeschuetz, J. W. Validating and understanding ring conformations using small molecule crystallographic data. *J. Chem. Inf. Model.* **52**, 956–962 (2012).

51. Varghese, F. S. *et al.* Berberine and Obatoclax Inhibit SARS-Cov-2 Replication in Primary Human Nasal Epithelial Cells In Vitro. *Viruses* **13**, (2021).

52. Gapsys, V. *et al.* Large scale relative protein ligand binding affinities using non-equilibrium alchemy. *Chem. Sci.* **11**, 1140–1152 (2019).

53. Maier, J. A. *et al.* ff14SB: Improving the Accuracy of Protein Side Chain and Backbone Parameters from ff99SB. *J. Chem. Theory Comput.* **11**, 3696–3713 (2015).

54. Crooks, G. E. Path-ensemble averages in systems driven far from equilibrium. *Phys. Rev. E* **61**, 2361–2366 (2000).

55. Bennett, C. H. Efficient estimation of free energy differences from Monte Carlo data. *J. Comput. Phys.* **22**, 245–268 (1976).

56. Salentin, S., Schreiber, S., Haupt, V. J., Adasme, M. F. & Schroeder, M. PLIP: fully automated protein-ligand interaction profiler. *Nucleic Acids Res.* **43**, W443–7 (2015).

Materials and Methods

1. Experimental methods

1.1 Fluorescence MPro inhibition assay

Compounds were seeded into assay-ready plates (Greiner 384 low volume, cat 784900) using an Echo 555 acoustic dispenser, and DMSO was back-filled for a uniform concentration in assay plates (DMSO concentration maximum 1%) Screening assays were performed in duplicate at 20μM and 50μM. Hits of greater than 50% inhibition at 50μM were confirmed by dose response assays. Dose response assays were performed in 12 point dilutions of 2-fold, typically beginning at 100μM. Highly active compounds were repeated in a similar fashion at lower concentrations beginning at 10μM or 1μM. Reagents for Mpro assay were dispensed into the assay plate in 10μl volumes for a final volume of 20μL.

Final reaction concentrations were 20mM HEPES pH7.3, 1.0mM TCEP, 50mM NaCl, 0.01% Tween-20, 10% glycerol, 5nM Mpro, 375nM fluorogenic peptide substrate ([5-FAM]-AVLQSGFR-[Lys(Dabcyl)]-K-amide). Mpro was pre-incubated for 15 minutes at room temperature with compound before addition of substrate and a further 30 minute incubation. Protease reaction was measured in a BMG Pherastar FS with a 480/520 ex/em filter set. Raw data was mapped and normalized to high (Protease with DMSO) and low (No Protease) controls using Genedata Screener software. Normalized data was then uploaded to CDD Vault (Collaborative Drug Discovery). Dose response curves were generated for IC50 using nonlinear regression with the Levenberg–Marquardt algorithm with minimum inhibition = 0% and maximum inhibition = 100%.

1.2 RapidFire MPro inhibition assay

The assay was performed according to the published procedure[37]. Briefly, compounds were seeded into assay-ready plates (Greiner 384PP, cat# 781280) using an ECHO 650T dispenser and DMSO was back-filled for a uniform concentration in assay plates (DMSO concentration < 1%, final volume = 500 nL.). A 15 μM enzyme stock solution is prepared in 20 mM HEPES, pH 7.5 and 300 mM NaCl, and subsequently diluted to a working solution of 300 nM Mpro in assay buffer (20 mM HEPES, pH 7.5 and 50 mM NaCl) before the addition of 25 μL to each well using a Multidrop Combi (Thermo Scientific). After a quick centrifugation step (1000 rpm, 15 s) the plate is incubated for 15 min at room temperature. The reaction is initiated with the addition of 25 μL of 4 μM 11-mer (TSAVLQSGFRK-NH2, initially custom synthesized by the Schofield group, GLBiochem, used until March 2021), or 10 μM 37-mer (ALNDFSNSGSDVLYQPPQTSITSAVLQSGFRKMAFPS-NH2, GLBiochem, used after March 2021), dissolved in assay buffer. After centrifugation (1000 rpm, 14 s) the reaction is incubated for 10 min (11-mer) or 5 min (37-mer) at room temperature before quenching with 10 % formic acid. The reactions are analysed with MS using RapidFire (RF) 365 high-throughput sampling robot (Agilent) connected to an iFunnel Agilent 6550 accurate mass quadrupole time-of-flight (Q-TOF) mass spectrometer using electrospray. All compounds are triaged by testing the % inhibition at 5 and 50 μM final concentration. Dose response curves uses an 11-point range of 100--0.0017 μM inhibitor concentrations. RapidFire integrator software (Agilent) was used to extract the charged states from the total ion chromatogram data followed by peak integration. For the 11-mer peptide the m/z (+1) charge states of both the substrate (1191.67 Da) and cleaved N-terminal product TSAVLQ (617.34 Da) were used and the 37-mer peptide the m/z (+2) charge states of the substrate (3960.94 Da) and m/z (+1) of the cleaved C-terminal product SGFRKMAFPS (1125.57 Da). Percentage conversion (product peak integral / (product peak integral + substrate peak integral))*100) and percentage inhibitions were calculated and normalised against DMSO control with deduction of any background signal in Microsoft Excel. IC50s were calculated using Levenberg–Marquardt algorithm used to fit a restrained Hill equation to the dose-response data with both GraphPad PRISM and CDD.

1.2 High throughput X-ray crystallography

Purified protein[13] at 24 mg/ml in 20 mM HEPES pH 7.5, 50 mM NaCl buffer was diluted to 12 mg/ml with 20 mM HEPES pH 7.5, 50 mM NaCl before performing crystallization using the sitting-drop vapour diffusion method with a reservoir solution containing 11% PEG 4 K, 5% DMSO, 0.1 M MES pH 6.5. Crystals of Mpro in the monoclinic crystal form (C2), with a single monomer in the asymmetric unit, were grown with drop ratios of 0.15 µl protein, 0.3 µl reservoir solution and 0.05 µl seeds prepared from previously produced crystals of the same crystal form[13]. Crystals in the orthorhombic crystal form ($P2_12_12_1$), with the Mpro dimer present in the asymmetric unit, were grown with drop ratios of 0.15 µl protein, 0.15 µl reservoir solution and 0.05 µl seeds prepared from crystals of an immature Mpro mutant in the same crystal form[38].

Compounds were soaked into crystals by adding compound stock solutions directly to the crystallisation drops using an ECHO liquid handler. In brief, 40-90 nl of DMSO solutions (between 20 and 100 mM) were transferred directly to crystallisation drops using giving a final compound concentration of 2-20 mM and DMSO concentration of 10-20%. Drops were incubated at room temperature for approx. 1-3 h prior to mounting and flash cooling in liquid nitrogen without the addition of further cryoprotectant.

Data was collected at Diamond Light Source on the beamline I04-1 at 100 K and processed with the fully automated pipelines at Diamond[39–41], which include XDS [42], xia2[43], autoPROC[44] and DIALS[39]. Further analysis was performed using XChemExplorer[45] with electron density maps generated using DIMPLE (http://ccp4.github.io/dimple/). Ligand-binding events were identified using PanDDA[46] (https://github.com/ConorFWild/pandda) and ligands were manually modelled into PanDDA-calculated event maps or electron density maps using Coot[47]. Ligand restraints were calculated with ACEDRG[48] or GRADE (grade v. 1.2.19 (Global Phasing Ltd., Cambridge, United Kingdom, 2010)) and structures refined with Buster (Buster v. 2.10.13 (Cambridge, United Kingdom, 2017)). Models and quality annotations were reviewed using XChemReview (citation?), Buster-Report (Buster v. 2.10.13 (Cambridge, United Kingdom, 2017)) and Mogul[49,50].

Coordinates, structure factors and PanDDA event maps for all data sets are available on Fragalysis (https://fragalysis.diamond.ac.uk/viewer/react/preview/target/Mpro).

1.3 Viral screening assays

A variety of antiviral replication assays were performed in collaborating laboratories, including cytopathic effect (CPE) inhibition assays at the IIBR, Israel, and the Neyts laboratory Katholieke Universiteit Leuven, viral qPCR at Radboud, Netherlands, immunofluorescence assays at University of Nebraska Medical centre, USA, and plaque assays and focus forming unit assays at University of Oxford, UK.

1.3.1 Antiviral Cytopathic Effect Assay, VeroE6 (IIBR, Ness-Ziona, Israel)

SARS-CoV-2 (GISAID accession EPI_ISL_406862) was kindly provided by Bundeswehr Institute of Microbiology, Munich, Germany. Virus stocks were propagated (4 passages) and tittered on Vero E6 cells. Handling and working with SARS-CoV-2 virus was conducted in a BSL3 facility in accordance with the biosafety guidelines of the Israel Institute for Biological Research (IIBR). Vero E6 were plated in 96-well plates and treated with compounds in medium containing 2 % fetal bovine serum. The assay plates containing compound dilutions and cells were incubated for 1 hour at 37°C temperature prior to adding Multiplicity of infection (MOI) 0.01 of viruses. Viruses were added to the entire plate, including virus control wells that did not contain test compound and Remdesivir drug used as positive control. After 72h incubation viral cytopathic effect (CPE) inhibition assay was measured with XTT reagent. Three replicate plates were used.

1.3.2 Antiviral Immunoflourescence assay, VeroE6 (Pathology and Microbiology, University of Nebraska Medical Centre, USA, St Patrick Reid)

Vero E6 cells were pretreated with 20 uM of the Moonshot compounds for around 2h. Cells were then infected with SARS-CoV-2 at a MOI of 0.1 for 24h. Virus infection was terminated by 4 % PFA fixation. Cells were stained using a Rabbit SARS-CoV-2 antibody (Sino Biological 40150-R007) as a primary antibody, and Alexa-488, Hoechst and Cell Mask (Thermo Fisher) as a secondary antibody. Images were collected on the Operetta system imaging system, and analysed using the Harmony software.

1.3.3 Antiviral Focus Forming Unit Assay, Calu-3 (University of Oxford, UK)

Cell culture. The African green monkey Vero E6 cell line (ATCC CRL-1586) was cultured in Dulbecco's modified Eagle medium (DMEM) with Glutamax supplemented with 100 µg/mL streptomycin, 100 U/mL penicillin, and 10 % heat-inactivated fetal calf serum (FCS). The human lung cancer cell line Calu-3 (Anderson Ryan, Department of Oncology, Medical Science Division, University of Oxford) was cultured in a 1:1 mixture of DMEM with Glutamax and Ham's F-12 medium supplemented with 100 µg/mL streptomycin, 100 U/mL penicillin, and 10 % heat-inactivated FCS. All cells were maintained as mycoplasma free, with regular verifications by polymerase chain reaction (PCR).

Virus propagation. SARS-CoV-2 England/2/2020 was provided at passage 1 from Public Health England, Collindale. Passage 2 submaster and passage 3 working stocks were produced by infecting Vero E6 cells at a multiplicity of infection of 0.01 in virus propagation medium (DMEM with Glutamax supplemented with 2 % FCS) and incubating until cytopathic effect was visible. The cell supernatant was then centrifuged at 500 g for 5 minutes, aliquoted and stored at -80°C. The titre of viral stocks was determined by plaque assay. All subsequent assays were performed using a passage 3 stock.

Cell viability. Cell viability was was measured using the CellTiter 96 R AQueous One Solution Cell Proliferation MTA (3-(4,5-dimethylthiazol-2-yl)-5-(3-carboxymethoxyphenyl)-2-(4-sulfophenyl)-2H - 15 tetrazolium, inner salt) Assay (Promega) according to the manufacturer's instruction after treatment with compound. Briefly, Calu 3 cells were treated with compounds in quadruplicate for 3 days. Wells with 200 µL growth medium with and without cells were included as controls in quadruplicate. After the incubation, 100 µL of growth medium was removed and 20 µL of MTS reagent was added to the remaining medium in each well. After a further one to two hour incubation, the absorbance at 490 nm was measured on a Molecular Devices SpectraMax M5 microplate reader.

Antiviral assays. For Focus forming unit assays, a SARS-CoV-2 Microneutralization assay from the W James lab (Dunn School of Pathology, University of Oxford) was adapted for use as a FFU assay. Briefly, 3 half log dilutions of each supernatant to be analyzed were prepared in virus propagation medium. 20µL of each dilution was inoculated into wells of a 96-well plate in quadruplicate followed by 100 µL Vero E6 cells at 4.5 x 10^5 cells/mL in virus propagation medium. The plates were incubated for 2 hours prior to the addition of 100 µL of 1.8 % CMC overlay, and then incubated for a further 24 hours. After 24 hours the overlay was carefully removed and the cells washed once with PBS before fixing with 50µL of 4 % paraformaldehyde, after 30 minutes the paraformaldehyde was removed and replaced with 100µL of 1 % ethanolamine in PBS. The cells were permeabilized by replacing the ethanolamine with 2 % Triton X100 in PBS and incubating at 37°C for 30 minutes. The plates were then washed 3 times with wash buffer (0.1 % Tween 20 in PBS) inverted and gently tapped onto tissue to dry before the addition of 50 µl of EY2A anti-N human mAb (Arthur Huang (Taiwan)/Alain Townsend (Weatherall Institute of Molecular Medicine, University of Oxford)) at 10 pmol in wash buffer. The plates were rocked at room temperature for 1 hour, washed and incubated with 100µl of secondary antibody Anti-Human IgG (Fc-specific)-peroxidase-conjugate produced in Goat diluted 1:5000 at room temperature for 1 hour. 50µL of TrueBlue peroxidase substrate was added to the wells and incubated at RT for 10 min on the rocker, after 10 minutes the substrate was removed and

the plates washed with ddH2O for 10 minutes. The H2O was removed and the plates allowed to air dry. The foci were then counted using an ELISPOT classic reader system (AID GmbH).

1.3.4 Antiviral qPCR assay, VeroE6 (Radboud University Medical Center, Nijmegen, Netherlands)

Cells African green monkey Vero E6 kidney cells (ATCC CRL-1586) and Vero FM kidney cells (ATCC CCL-81) were cultured in Dulbecco's modified Eagle medium (DMEM) with 4.5g/L glucose and L-glutamine (Gibco), supplemented with 10\% Fetal calf serum (FCS, Sigma Aldrich), 100 µg/ml streptomycin and 100 U/ml penicillin (Gibco). Cells were maintained at 37℃ with 5 % CO2.

Virus. SARS-CoV-2 (isolate BetaCoV/Munich/BavPat1/2020) was kindly provided by Prof. C. Drosten (Charité-Universitätsmedizin Berlin Institute of Virology, Berlin, Germany) and was initially cultured in Vero E6 cells up to three passages in the laboratory of Prof. Bart Haagmans (Viroscience Department, Erasmus Medical Center, Rotterdam, The Netherlands). Vero FM cells were infected with passage 3 stock at an MOI of 0.01 in infection medium (DMEM containing L-glutamine, 2 % FCS, 20 mM HEPES buffer, 100 µg/ml streptomycin and 100 U/ml penicillin). Cell culture supernatant containing virus was harvested at 48 hours post-infection (hpi), centrifuged to remove cellular debris, filtered using a 0.2 0 µm syringe filter (Whatman), and stored in 100 µl aliquots at -80℃.

Virus stock titration. Vero E6 cells were seeded in 12-well plates at a density of 500,000 cells/well. Cell culture medium was discarded at 24 h post-seeding, cells were washed twice with PBS and infected with 10-fold dilutions of the virus stock. At 1 hpi, cells were washed with PBS and replaced with overlay medium containing Minimum Essential medium (MEM), 2 % FCS, 20mM HEPES buffer, 100 µg/ml streptomycin, 100 U/ml penicillin and 0.75 % carboxymethyl cellulose (Sigma Aldrich). At 48 hpi, the overlay medium was discarded, cells were washed with PBS and stained with 0.25 % crystal violet solution containing 4 % formaldehyde for 30 minutes. Thereafter, staining solution was discarded, plates washed with double-distilled water, dried and plaques were counted.

Antiviral assay. Vero E6 cells were seeded onto 24-well plates at a density of 150,000 cells/well. At 24 h post-seeding, cell culture medium was discarded, cells were washed twice with PBS and infected with SARS-CoV-2 at an MOI of 0.01 in the presence of six concentrations of the inhibitors (25 µM – 0.06 µM). At 1 hpi, the inoculum was discarded, cells were washed with PBS, and infection medium containing the same concentration of the inhibitors was added to the wells. SARS-CoV-2 infection in the presence of 0.1 % DMSO was used as a negative control. At 24 hpi, 100 µl of the cell culture supernatant was added to RNA-Solv reagent (Omega Bio-Tek) and RNA was isolated and precipitated in the presence of glycogen according to manufacturer's instructions. qRT-PCR. TaqMan Reverse Transcription reagent and random hexamers (Applied Biosystems) were used for cDNA synthesis. Semi-quantitative real-time PCR was performed using GoTaq qPCR (Promega) BRYT Green Dye-based kit using primers targeting the SARS-CoV-2 E protein gene (Forward primer, 5′-ACAGGTACGTTAATAGTTAATAGCGT-3'; Reverse primer, 5′-ACAGGTACGTTAATAGTTAATAGCGT-3'). A standard curve of a plasmid containing the E gene qPCR amplicon was used to convert Ct values relative genome copy numbers. Vero E6 cells were seeded in 96-well white-bottom culture plates (Perkin Elmer) at a density of 30,000 cells per well. At 24 h post-seeding, cells were treated with the same concentrations of compounds as used for the antiviral assay. Cells treated with 0.1 % DMSO were used as a negative control. At 24 h post-treatment, cell viability was assessed using the Cell Titer Glo 2.0 kit (Promega) using the Victor Multilabel Plate Reader (Perkin Elmer) to measure luminescence signal.

Organoid assays. Organoids were infected with SARS-CoV-2 in transwell filters (Corning) using a multiplicity of infection (MOI) of 1.0 in E6 medium for 4 h at 37°C, 5% (v/v) CO_2 exposing both basolaterally and apically as described previously[51]. . Medium containing virus was replaced for E6 medium and cultured for an additional 5 days. After 5 days, organoids were washed in PBS, harvested and processed for further analysis. For antiviral assays, organoids were infected with SARS-CoV-2 at an MOI of 1 in the presence of

10 μM MAT-POS-b3e365b9-1 or 0.1% DMSO. MAT-POS-b3e365b9-1. Organoids were harvested at 48 and 96 hpi, and supernatant from the apical compartment harvested at 96 hpi, were analyzed by RT-qPCR and plaque assays as described previously[51]. Antiviral activity on Vero E6 cells was tested by inoculating cells at an MOI of 0.01 for 1 h, after which the cells were washed with PBS and treated with a serial dilution of MAT-POS-b3e365b9-1 in DMEM. The supernatant was harvested at 24 hpi for RNA isolation using the QIAamp viral RNA mini kit (Qiagen) and RT-qPCR. CellTiter-Glo assay (Promega) was used to assess cell viability (in absence of infection).

1.3.5 High-content SARS-CoV-2 antiviral screening assay, Hela-ACE2 (Takeda via Calibr/TSRI)

SARS-CoV-2/HeLa-ACE2 high-content screening assay. Compounds are acoustically transferred into 384-well μclear-bottom plates (Greiner, Part. No. 781090-2B) and HeLa-ACE2 cells are seeded in the plates in 2% FBS at a density of 1.0×10^3 cells per well. Plated cells are transported to the BSL3 facility where SARS-CoV-2 (strain USA-WA1/2020 propagated in Vero E6 cells) diluted in assay media is added to achieve ~30 – 50% infected cells. Plates are incubated for 24 h at 34℃ 5% CO_2, and then fixed with 8% formaldehyde. Fixed cells are stained with human polyclonal sera as the primary antibody, goat anti-human H+L conjugated Alexa 488 (Thermo Fisher Scientific A11013) as the secondary antibody, and antifade-46-diamidino-2-phenylindole (DAPI; Thermo Fisher Scientific D1306) to stain DNA, with PBS 0.05% Tween 20 washes in between fixation and subsequent primary and secondary antibody staining. Plates are imaged using the ImageXpress Micro Confocal High-Content Imaging System (Molecular Devices) with a 10× objective, with 4 fields imaged per well. Images are analyzed using the Multi-Wavelength Cell Scoring Application Module (MetaXpress), with DAPI staining identifying the host-cell nuclei (the total number of cells in the images) and the SARS-CoV-2 immunofluorescence signal leading to identification of infected cells.

Uninfected host cell cytotoxicity counter screen. Compounds are acoustically transferred into 1,536-well plates (Corning No. 9006BC). HeLa-ACE2 cells are maintained as described for the infection assay and seeded in the assay-ready plates at 400 cells/well in DMEM with 2% FBS. Plates are incubated for 24 hours at 37℃ 5% CO_2. To assess cell viability, 2 mL of 50% Cell-Titer Glo (Promega No G7573) diluted in water is added to the cells and luminescence measured on an EnVision Plate Reader (Perkin Elmer).

Data analysis. Primary in vitro screen and the host cell cytotoxicity counter screen data are uploaded to Genedata Screener, Version 16.0. Data are normalized to neutral (DMSO) minus inhibitor controls (2.5 μM remdesivir for antiviral effect and 10 μM puromycin for infected host cell toxicity). For the uninfected host cell cytotoxicity counter screen 40 μM puromycin (Sigma) is used as the positive control. For dose response experiments compounds are tested in technical triplicates on different assay plates and dose curves are fitted with the four parameter Hill Equation.

1.3.6 Cytopathic Effect Assay, hACE2-TMPRSS2 **cells (Katholieke Universiteit Leuven)**

Virus isolation and virus stocks All virus-related work was conducted in the high-containment BSL3 facilities of the KU Leuven Rega Institute (3CAPS) under licenses AMV 30112018 SBB 219 2018 0892 and AMV 23102017 SBB 219 2017 0589 according to institutional guidelines. The Severe Acute Respiratory Syndrome Coronavirus 2 (SARS-CoV-2) strain used for this study was the Alpha variant of Concern (derived from hCoV-19/Belgium/rega-12211513/2020; EPI_ISL_791333, 2020-12-21). Virus sample was originally isolated in-house from nasopharyngeal swabs taken from travelers returning to Belgium (baseline surveillance) and were subjected to sequencing on a MinION platform (Oxford Nanopore) directly from the nasopharyngeal swabs. Virus stocks were then grown on Vero E6 cells in (DMEM 2% FBS medium) and passaged one time on A549-ACE2TMPRSS2 cells. Median tissue culture infectious doses (TCID50) was defined by end-point titration.

A549-ACE2-TMPRSS2 assay A549-Dual™ hACE2-TMPRSS2 cells obtained by Invitrogen (Cat. a549d-cov2r) were cultured in DMEM 10% FCS (Hyclone) supplemented with 10 μg/ml blasticidin

(Invivogen, ant-bl-05), 100 µg/ml hygromycin (Invivogen, ant-hg-1), 0.5 µg/ml puromycin (Invivogen, ant-pr-1) and 100 µg/ml zeocin (Invivogen, ant-zn-05). For antiviral assay, cells were seeded in assay medium (DMEM 2%) at a density of 15,000 cells/well. One day after, compound was serially diluted in assay medium (DMEM supplemented with 2% v/v FCS) and cells were infected with their respective SARS-CoV-2 strain at a MOI of approximately 0.003 TCID50/ml. On day 4 pi., differences in cell viability caused by virus-induced CPE or by compound-specific side effects were analyzed using MTS as described previously [1].Cytotoxic effects caused by compound treatment alone were monitored in parallel plates containing mock-infected cells.

2. Computational methods

2.1 Synthetic route planning

We employ an approach based on the Molecular Transformer technology[22]. Our algorithm uses natural language processing to predict the outcomes of chemical reactions and design retrosynthetic routes starting from commercially available building blocks. This proprietary platform is provided free of charge by PostEra Inc (http://postera.ai). Additionally, Manifold (https://postera.ai/manifold) was built by PostEra Inc. during the project to search the entire space of purchasable molecules, and automatically find the optimal building blocks.

2.2 Alchemical free energy calculations

Large-scale alchemical free energy calculations were conducted in “Sprints” in which each set of calculations aimed to prioritize compounds that could be produced from a common synthetic intermediate using Enamine’s extensive building block library, resulting in synthetic libraries of hundreds to tens of thousands. Virtual synthetic libraries were organized into a star map, where all transformations were made with respect to a single reference X-ray structure and compound with experimentally measured bioactivity. X-ray structures were prepared using the OpenEye Toolkit SpruceTK with manually controlled protonation states for the key His61:Cys145 catalytic dyad (variously using zwitterionic or uncharged states). Initial poses of target compounds were were generated via constrained conformer enumeration to identify minimally-clashing poses using Omega (from the OpenEye Toolkit) using a strategy that closely follows an exercise described in a blog post by Pat Walters (http://practicalcheminformatics.blogspot.com/2020/03/building-on-fragments-from-diamondxchem_30.html) . Alchemical free energy calculations were then prepared using the open source perses relative alchemical free energy toolkit[30] (https://github.com/choderalab/perses), and nonequilibrium switching alchemical free energy calculations[52] were run on Folding@home using the OpenMM compute core[31]. Nonequilibrium switching calculations used 1 ns nonequilibrium alchemical trajectories, where most calculations were performed with 1 fs timesteps without constraints to hydrogen due to technical limitations that have been resolved in calculations employing OpenMM 7.5.1 and later. We used the Open Force Field Initiative OpenFF “Parsley” small molecule force fields[29] (multiple generations were released and used as the project evolved) and the AMBER14SB protein force field[53] with recommended ion parameters, and TIP3P water. Calculations were analyzed using the fah-xchem dashboard (https://github.com/choderalab/fah-xchem) using the Bennett acceptance ratio[54,55] (https://threeplusone.com/pubs/gecthesis) and posted online in real time for the medicinal chemistry team to consult in making decisions about which compounds to prioritize.

Scripts for performing and analyzing alchemical free energy calculations, as well as an index of computed datasets and dashboards are available at https://github.com/foldingathome/covid-moonshot

Code for generating the COVID Moonshot alchemical free energy calculation web dashboards is available here: https://github.com/choderalab/fah-xchem

2.3 Structural flexibility and interactions analysis

Protein-ligand interactions are the driving forces for molecular recognition. In this work, the *plipify* repo (https://github.com/volkamerlab/plipify) is used to detect shared interaction hot spots within the different MPro structures. plipify is a python wrapper built on top of PLIP[56], a tool that enables automatic generation of protein-ligand interaction profiles for single complexes, to allow combining these profiles for multiple structures.

To generate the hotspots (depicted in **Figure 3A**), the fragalysis data was downloaded (as of July 2021, https://fragalysis.diamond.ac.uk/api/targets/?format=json&title=Mpro). The respective 493 pre-aligned complex structures were further investigated (found under data/{target}/aligned/{crystal_name}/{crystal_name}_bound.pdb). Only one chain per structure is kept, and the structures are protonated using Amber's *reduce* function. Plipify is invoked and structures are excluded from further analysis if they do contain exactly one binding site (i.e. PLIP detects either zero or more than 1 binding sites), the sequence contains gaps ('-') or the sequence length differs more than a standard deviation from the average length across all investigated structures.

This resulted in a final set of 391 complex structures, used to generate the interaction fingerprints. Note for this study, only hbond-donor, hbond-acceptor, salt bridge, hydrophobic, pistacking, and halogen interactions are inspected. Interacting residues are only included if the summed interaction count per residue over all investigated structures is greater than five. The resulting structural depiction (**Figure 3A**) were generated using pymol , and structure Mpro-P0157_0A_bound_chainA (protonated) is displayed (scripts available at https://github.com/volkamerlab/plipify/projects/01/fragalysis.ipynb).

Scripts used to generate structural **Figure 1A**, **Figure 3B**, and **Supplementary FIgure 1B** are available at https://github.com/choderalab/covid-moonshot-manuscript/

Supplementary Figures

Supplementary Figure 1: The SARS-CoV-2 main viral protease (Mpro) is highly conserved across coronaviruses.
A: Mpro sequences across coronaviruses are highly conserved due to their requirement to cleave viral polyproteins in numerous locations, showing very little variation in residues lining the active site near the scissile bond.
B: Available structural data for Mpro from multiple coronaviruses shows a high degree of structural conservation, especially in the vicinity of the active site.

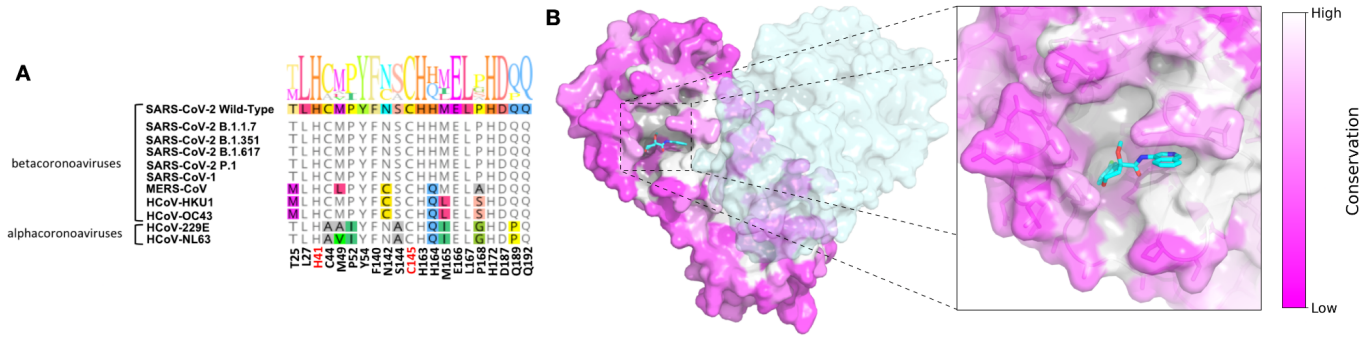

Supplementary Figure 2: Our lead compounds, PET-UNK-29afea89-2 and MAT-POS-932d1078-3, demonstrate antiviral activity across different cell lines. The figure shows dose-response curve in Immunofluorescence assays Hela-ACE2 cells, Focus Forming Unit assays in Calu-3 cells and Cytopathic Effect assays in A549-ACE2-TMPRSS2 cells. The curves also show the cytotoxicity data (dotted lines), demonstrating the lack of cytotoxic activity across all three cell lines .

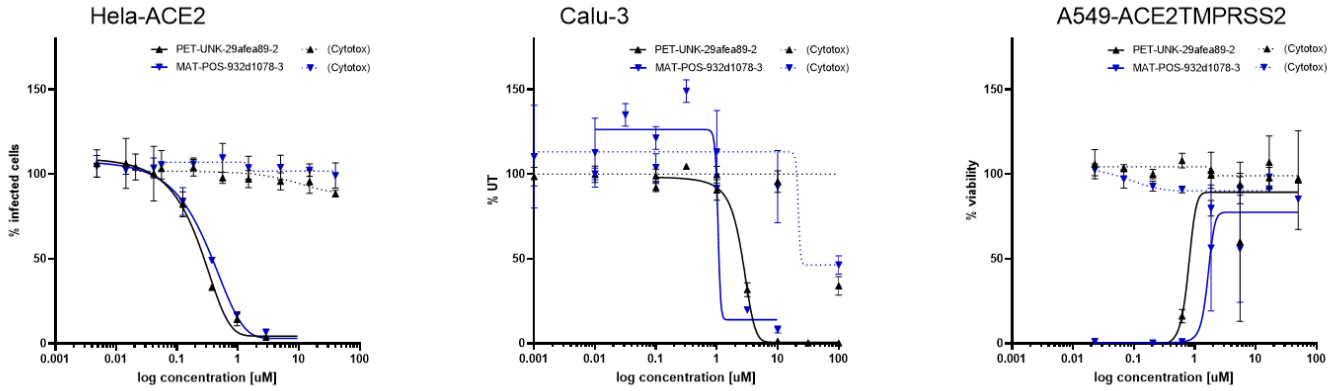

Supplementary Table 1: MAT-POS-932d1078-3 is profiled across different ADME measurements, demonstrating its potential as a developable oral therapeutic.

Property	Measurement
Aqueous kinetic solubility	375 uM
Rat microsomes Clint	70.1 ± 1.25 (ul/min/mg)
Rat microsomes t 1/2	24.7 ± 0.441 (min)
Dog microsomes Clint	44.8 ± 0.447 (ul/min/mg)
Dog microsomes t 1/2	38.7 ± 0.387 (min)
Human microsomes Clint	25.3 ± 0.901 (ul/min/mg)
Human microsomes t 1/2	68.6 ± 2.45 (min)
Rat hepatocytes Clint	24.6 ± 0.226 (ul/min/mg)
Rat hepatocytes t 1/2	56.4 ± 0.519 (min)
Human hepatocytes Clint	11.6 ± 0.744 (ul/min/mg)
Human hepatocytes t 1/2	60.0 ± 3.86 (min)
PPB human	89.6%
PPB rat	79.3%
Rat PK, IV (2 mg/kg)	AUC = 594 ng h/ml, T1/2 = 1.17 h, Clint = 56.9 ml/min/kg, Vdss = 3.48 L/kg
Rat PK, PO (10 mg/kg)	AUC = 792 ng h/ml, T1/2 = 2.86 h, Cmax = 205 ng/ml, Tmax = 0.833h, BA=31%